Tunable Spectral Ordering of Magnetic Plasmon Resonances

Nicholas P. Montoni, Steven C. Quillin, Charles Cherqui, and David J. Maisello*

Department of Chemistry, University of Washington, Seattle, WA 98195

E-mail: masiello@chem.washington.edu

Abstract

Abstract.

Keywords

magnetic plasmons, plasmon metamolecules, plasmon oligomers

Plasmon oligomers, or plasmon metamolecules, are clusters of noble metal nanoparticles (MNPs) that exhibit anomalously strong magnetic fields even though their individual nanoparticle building blocks do not. Since their discovery in 2004, such magnetic plasmon resonances have impacted a variety of applied and fundamental research from negative index metamaterials to quantum tunneling and Fano interferences.[1–10] Magnetic plasmons have been shown to couple to and enhance the magnetic field of light and hybridize analogously to electric plasmon resonances.[7,10–15] The magnetic properties of single oligomers, i.e. those clusters composed of only one ring of MNPs, are now well understood based upon quasistatic models.[6,9,16,17] So too are extendend two-dimensional networks of oligomers using quasistatic tight-binding models.[18,19] However, recently, a disconnect between these extremes and methods has been highlighted, revealing a lack of understanding of how oligomer assemblies behave in the so-called intermediate size regime.[7,10,13–15,20,21]

Most crucial to this disconnect is the question of when and how retardation effects matter. For example, in the case of the two oligomer cluster the quasistatic approximation has been shown to deviate from full-wave numerical electrodynamics simulations in that it predicts a different energy-ordering of the two magnetic plasmon resonances.[7] Retardation effects have been incorporated into models of single MNPs,[22] dimers,[23,24] and infinite chains and arrays.[18,25–35] However, with the exception of numerical studies, no analytical models to date include retardation effects in the description of magnetic plasmon resonances. It is the purpose of this paper to show that the incorporation of retardation effects corrects the aforementioned disagreement between model and simulation, and further points to the facile ability to tune the magnetic plasmon spectrum by changing the oligomer's size. The latter observation is important because it enables manipulation of the system's effective permittivity and permeability, thereby facilitating the design of future tunable optical metamaterials.

In the following, we build a simple analytically-solvable model to demonstrate the size-dependent evolution of the magnetic plasmons in intermediate-size N-mers by including the effects of retardation in the mutual interaction of their underlying electric dipole plasmon resonances. Interestingly, as a function of size, the magnetic plasmons switch their ordering in analogy to the way that electric plasmons in hybridized nanoparticles switch order.[24] We further analyze the distinct radiative properties of these magnetic plasmons by computing the angle-resolved cathodoluminescence (CL) spectrum.[36–39] Building from the intuition gained, we finally analyze the size-dependent evolution of the intermediate-size plasmonic nanoclusters measured in Ref.[15] We find that the spectral ordering depends not only on aggregate size but also upon morphology, offering the ability to tune the magnetic plasmon spectrum. Such understanding may someday lead to advances in superlensing and electromagnetic cloaking at optical frequencies, as these applications benefit directly from the tunability of system's electric and magnetic response.[40–47]

1 Model Theory

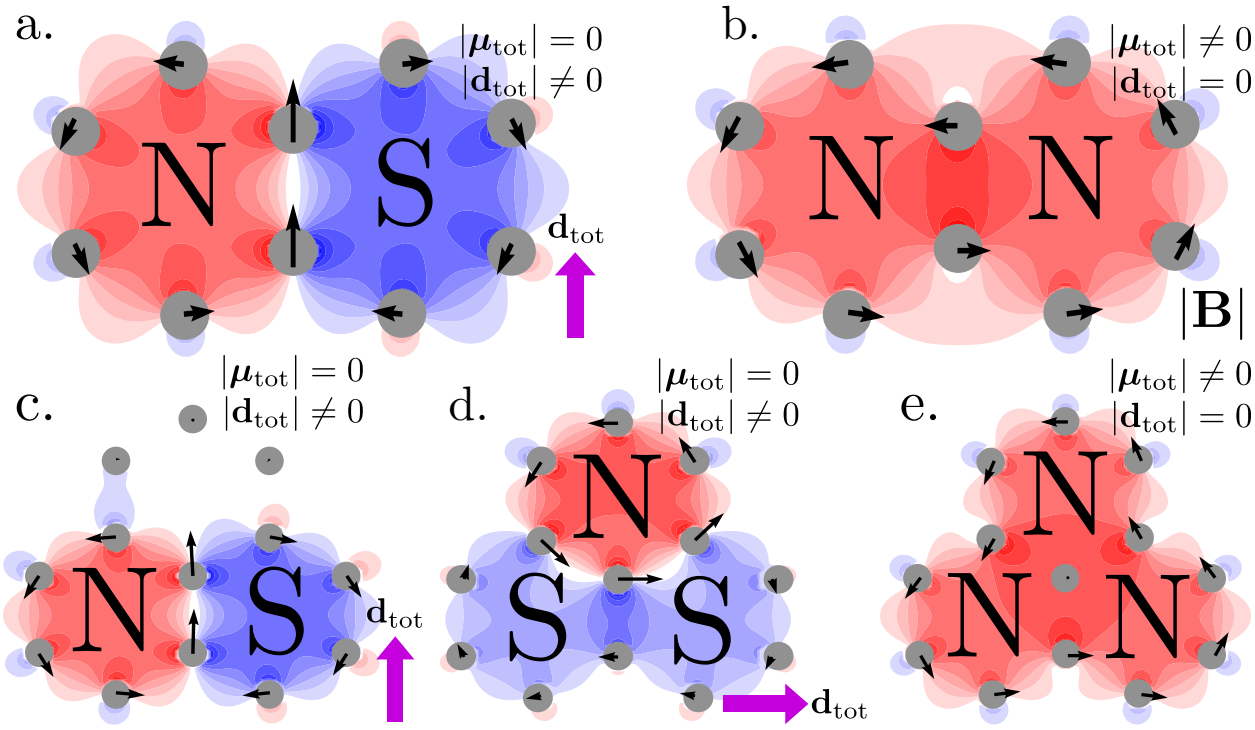

Figure 1: Magnetic field plots of the 2mer (a and b) and 3mer (c, d, and e) oligomers. Each system supports a number of closed-loop magnetic plasmon resonances equal to the number of rings in the system. The magnetic plasmons support an electric dipole moment (a, c, and d) support out-of-phase magnetic fields. The nodeless magnetic modes (b and e) support a net magnetic dipole moment are accessible to the magnetic field of light.

Fig. 1 displays two model oligomer systems, the 2-mer and 3-mer, comprising 10 and 13 silver nanospheres in analogy to the molecules naphthalene and phenalene. Mapping the electric plasmons of each nanoparticle onto harmonic oscillators is now well-understood,[7,48] and forms the basis for modeling the collective magnetic plasmon responses. In the limit where each nanoparticle, here restricted to a spherical geometry of radius a, possesses only an electric dipole plasmon resonance, the equations of motion dictating the electromagnetic behavior of the oligomer are

$$\ddot{\mathbf{q}}_i + \omega_{\text{sp}}^2 \mathbf{q}_i = \frac{e}{m_{\text{sp}}} \sum_{j \neq i} \mathbf{E}_j(\mathbf{r}_i), \tag{1}$$

where $\omega_{\rm sp} = \sqrt{\omega_p^2/(\varepsilon_\infty + 2\varepsilon_b) - (\gamma/2)^2}$ is the complex Mie resonance frequency and $m_{\rm sp} = e^2/\alpha_{\rm sp}\omega_{\rm sp}^2$ is the plasmon's effective mass defined in terms of the polarizability $\alpha_{\rm sp} = 3a^3/(\varepsilon_\infty + 2\varepsilon_b)$. Here, ω_p is the metal's bulk plasma frequency, ε_∞ and ε_b are the high-frequency and background dielectric functions, and γ is well approximated by the Drude electron-ion scattering rate for the nanoparticle sizes under consideration. While the Drude frictional force is not explicitly included in the equations of motion, Drude friction does modify the frequency of the Mie resonance. The dipole moment $\mathbf{d}_i = e\mathbf{q}_i$ of each plasmon oscillator is restricted to lie in the plane of the oligomer at position $\mathbf{r}_i$, and $\mathbf{E}_j(\mathbf{r}_i)$ is the fully retarded electric field of the jth dipole evaluated at the position of the ith dipole. The electric field is defined by

$$\mathbf{E}_j(\mathbf{r}_i) = \mathbf{\Lambda}_{ij} \cdot \mathbf{d}_j = \left\{ \left(\frac{1}{r_{ij}^3} - \frac{ik}{r_{ij}^2} \right) (3\hat{\mathbf{n}}_{ij}\hat{\mathbf{n}}_{ij} - \mathbf{1}) - \frac{k^2}{r_{ij}} (\hat{\mathbf{n}}_{ij}\hat{\mathbf{n}}_{ij} - \mathbf{1}) \right\} \frac{e^{ikr_{ij}}}{\varepsilon_b} \cdot \mathbf{d}_j, \qquad (2)$$

where $\hat{\mathbf{n}}_{ij}$ is the unit vector connecting two dipoles separated by distance $r_{ij} = |\mathbf{r}_i - \mathbf{r}_j|$ and $k = \sqrt{\varepsilon_b}\omega/c$. The field is decomposed into three parts—the near- (r_{ij}^{-3}), intermediate- (r_{ij}^{-2}), and far-field (r_{ij}^{-1})—which together include all dipolar retardation effects.[49] Interestingly, the latter term carries the opposite sign of the former two. As will be shown in the following, it is because of both the relative magnitude and sign of these terms as well as the oscillatory behavior of $e^{ikr_{ij}}$ that the interactions can change character and switch from energy-lowering to energy-raising.

As described in the Methods Section, there are as many hybridized modes of each N-mer as there are electric dipole plasmons. Of these hybrid modes, some are electric and some are magnetic in character, with N magnetic plasmon resonances for each N-mer studied here. Fig. 1 shows the magnetic plasmon modes of the 2-mer and 3-mer overlaid with their associated signed magnetic field magnitude. Each mode is named for its particular magnetic field distribution after the poles of a magnet, either all-North (aN) or North-South (NS). The top right-hand corner of each panel indicates the net electric or magnetic dipole moment magnitude. The black arrows denote the electric dipole plasmons on each MNP within each

magnetic mode, while the magenta arrow indicates the mode's net electric dipole moment. In planar geometries, the magnetic dipole moments are always perpendicular to the in-plane electric dipole moments. As a result, they scatter light with different directionality as will be discussed.

2 Spectral Ordering of Magnetic Modes in Intermediate-Size N-mers

To determine the impact of incorporating retardation effects, it is first useful to consider the quasistatic limit. Here individual nanoparticle plasmon resonance frequencies (ω_{sp}) are size independent and the coupling strength depends only upon the scale $s_{ij} = r_{ij}/a$ and not upon the overall oligomer size. That is, if this ratio s_{ij} of interparticle distance r_{ij} to nanoparticle radius a remains constant, the collective resonance frequencies do not change as the nanoparticles grow. This is evident by considering the $ka \ll 1$ limit of the right-hand side of Eq. (1) [CHECK UNITS],

$$\begin{aligned}\lim_{ka\to 0} \frac{e}{m_{\mathrm{sp}}}\mathbf{E}_j(\mathbf{r}_i) &= \frac{e^2}{m_{\mathrm{sp}}}\mathbf{\Lambda}_{ij}\cdot\mathbf{q}_j \\ &= \frac{\omega_{\mathrm{sp}}^2\alpha_{\mathrm{sp}}^2}{\varepsilon_b}\frac{3\hat{\mathbf{n}}_{ij}\hat{\mathbf{n}}_{ij}-\mathbf{1}}{r_{ij}^3}\cdot\mathbf{q}_j \\ &= \frac{\omega_{\mathrm{sp}}^2}{\varepsilon_b}\left(\frac{3}{\varepsilon_\infty+2\varepsilon_b}\right)\frac{3\hat{\mathbf{n}}_{ij}\hat{\mathbf{n}}_{ij}-\mathbf{1}}{s_{ij}^3}\cdot\mathbf{q}_j.\end{aligned} \tag{3}$$

Retardation effects, however, remove this invariance and introduce radius-dependence into both the Mie frequency and the electric field. Consequently, in the following, we choose the individual MNP radius a as the independent variable, fixing the nearest neighbor distance at $3a$ to investigate the effects of retardation upon the magnetic plasmon spectrum in intermediate-size N-mers.

Fig. 2 shows the predicted magnetic plasmon resonance energies from both Eq. (1)

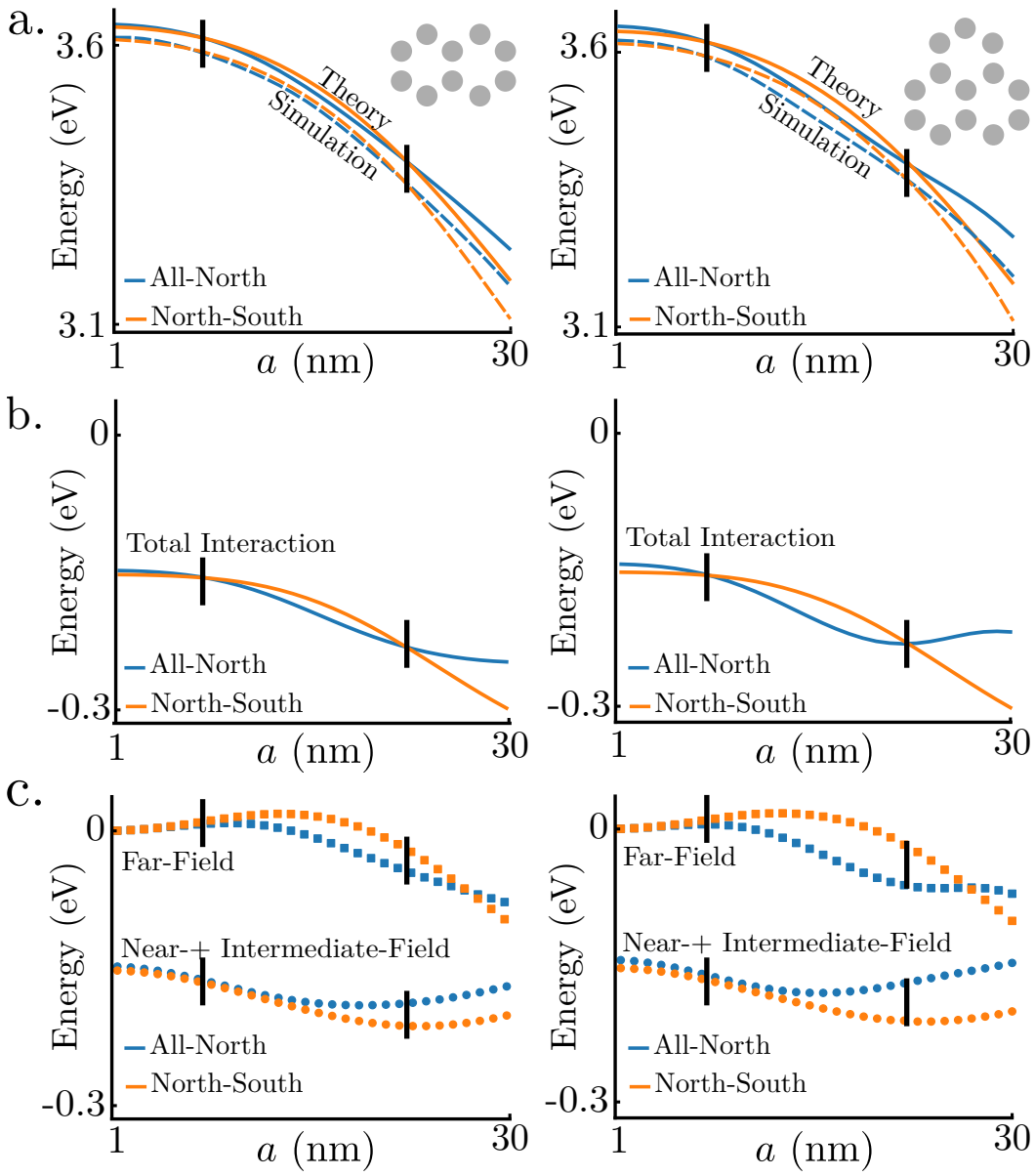

Figure 2: Eigenenergies (a and c) and interaction energies (b and d) for the 2mer and 3mer. At small scales $r_0 < 5$ nm the magnetic modes are ordered as predicted using a quasistatic model, with NS (orange) lower in energy than aN (blue). This implies that for very small oligomer systems, the quasistatic approximation is still accurate. However, at sizes greater than $r_0 = 5$ nm and smaller than $r_0 = 20$ nm, the eigenmodes switch order. This is due to the dominance of the far-field term, which is evident from (b and d). Finally, at sizes greater than $r_0 = 20$ nm, the eigenmodes switch order again. Also plotted are simulated peak positions of each mode (dashed lines) to show agreement within 0.1 eV.

and full-wave numerical electrodynamics simulation of the 2-mer and 3-mer with increasing a.[50] At small a, the magnetic modes preserve the quasistatic ordering predicted in previous work,[7] which is to be expected when the oligomer system fits within an optical wavelength and the near-field dominates the electric field. As the system size increases, the resonance energies decrease and cross at $a \approx 7$ nm, and once more at $a \approx 20$ nm. The second crossing recovers the same spectral ordering as at small sizes, which might lead to the erroneous conclusion that the quasistatic approximation is correct again. Rather, both crossings are due entirely to retardation effects as can be seen from the total interaction energy

$$U = -\frac{1}{2}\sum_{ij} \mathbf{d}_i \cdot \mathbf{E}_j(\mathbf{r}_i), \tag{4}$$

between each pair of electric dipole plasmons within each magnetic plasmon mode. It is the inclusion of the far-field that causes the mode switching, as it carries the opposite sign of the near- and intermediate-field terms. Fig. 2 shows the competition between these field components as well as their relative contributions to the total interaction energy. Inspection of Fig. 2c reveals that the crossing points occur where the splitting in the near- and intermediate-fields is equal and opposite to that of the far-field. Perhaps more interestingly, in any dielectric medium with $\varepsilon_b > 1$ the crossing points are shifted towards smaller scale due to wavelength contraction. This can be explained through the impact of dielectric medium upon the interaction energy U, which increases with increasing ε_b due mostly to the far-field term's dependence upon k^2.[51] While previous work has explored the oscillatory nature of hybridized electric dipole plasmon resonances and radiation damping as a function of separation in noble metal dimers,[24] our work shows that magnetic plasmon resonances also oscillate with interparticle separation and can be understood by analysis of the different contributions to the dipole-dipole interaction.

3 Radiative Properties of Intermediate-Size N-mers

Only those magnetic resonances that have net electric or magnetic dipole moments will couple strongly to the radiation field. The magnetic dipole moment of the aN magnetic mode is perpendicular to the electric dipole moment(s) of the NS mode in both the 2-mer and 3-mer. This means that these modes radiate with different directionality. It has been predicted and shown experimentally that 1-mers scatter light anisotropically when both their magnetic and electric dipole moments are mutually excited,[6,10] as is evident in differential scattering spectra and radiation profiles. Both observations stem from the time-averaged differential power,[52,53]

$$\frac{dP(\mathbf{x})}{d\Omega} = \frac{c}{8\pi}\mathrm{Re}\left[r^2\hat{\mathbf{n}}\cdot\sum_I \mathbf{E}_I(\mathbf{x})\times\sum_J \mathbf{B}_J^*(\mathbf{x})\right] \tag{5}$$

observed at the point $\mathbf{x} = r\hat{\mathbf{n}}$, where I, J label the 1-mer unit cells within each N-mer. $\mathbf{E}_I$ and $\mathbf{B}_I$ are produced from the sum of effective electric ($\mathbf{d}_I$) and magnetic ($\boldsymbol{\mu}_I$) dipole moments, assumed to be co-located at the center of the Ith ring and oscillating in time as $e^{-i\omega t}$. In this approximation, the differential power becomes[3]

$$\begin{aligned}\frac{dP(\mathbf{x})}{d\Omega} &= \frac{ck^4}{8\pi}\mathrm{Re}\left\{\hat{\mathbf{n}}\cdot\left[\left(\sum_i(\hat{\mathbf{n}}\times\mathbf{d}_I)\times\hat{\mathbf{n}} - \hat{\mathbf{n}}\times\boldsymbol{\mu}_I\right)\times\left(\sum_j \hat{\mathbf{n}}\times\mathbf{d}_J^* + (\hat{\mathbf{n}}\times\boldsymbol{\mu}_J^*)\times\hat{\mathbf{n}}\right)\right]\right\} \\ &= \frac{ck^4}{8\pi}\mathrm{Re}\Bigg[\sum_{ij}\mathbf{d}_I\cdot\mathbf{d}_J^* - (\hat{\mathbf{n}}\cdot\mathbf{d}_I)(\hat{\mathbf{n}}\cdot\mathbf{d}_J^*) + \boldsymbol{\mu}_I\cdot\boldsymbol{\mu}_J^* - (\hat{\mathbf{n}}\cdot\boldsymbol{\mu}_I)(\hat{\mathbf{n}}\cdot\boldsymbol{\mu}_J^*) \\ &\qquad + \hat{\mathbf{n}}\cdot(\mathbf{d}_I\times\boldsymbol{\mu}_J^* + \mathbf{d}_J^*\times\boldsymbol{\mu}_I)\Bigg].\end{aligned} \tag{6}$$

Notice that the first two terms are due to the radiation produced by electric and magnetic dipoles, while the third term is due to their interference. To build intuition, we define the magnetic dipole moment $\boldsymbol{\mu}$ to point in the z-direction and the electric dipole $\mathbf{d}$ to point in the y-direction for all I, J. The effective electric and magnetic dipoles can be written in terms

of their constituent dipoles as $\mathbf{d}_I = \sum_i d_{I,i}\hat{\mathbf{y}}$ and $\boldsymbol{\mu}_I = (k/2)\sum_i \mathbf{r}_i \times d_{I,i}\hat{\boldsymbol{\phi}}_i = (knRd_{I,i}/2)\hat{\mathbf{z}}$, where R is the radius of the 1-mer ring consisting of n nanoparticles, and $d_{I,i}$ is the electric dipole moment of the ith nanoparticle within the Ith unit cell. For each I, all $d_{I,i}$ are equal.

Fig. 3 displays the differential scattering power profiles associated with the aN (a) and NS (b) magnetic plasmon resonances as well as their interference (c) for any N-mer with electric and magnetic dipoles oriented as descibed above. Since the aN mode has only a z-oriented magnetic dipole, its radiation pattern is orthogonal to that of the y-directed electric dipole of the NS mode. This means that asymmetry in the radiation pattern is due to the excitation of both modes. Thus, examination of the radiation directionality allows one to determine the net electric or magnetic dipole character. Such forward/backward scattering asymmetries have been predicted and demonstrated in metal-semiconductor core-shell nanoparticle assemblies, that similarly exploit the interference between electric and magnetic plasmons to direct light.[54]

Recent studies have demonstrated the utility of angle-resolved CL spectroscopy to characterize plasmon resonances in noble metal nanoparticles.[37–39] Using an electron microscope fitted with a parabolic mirror, emitted CL radiation can be collected across a large portion of the backward scattering hemisphere.[37–39] Here we show that with the selection rules imposed by the location of the electron beam and the specific directionality of light emission, the size-dependent spectral order of the N-mers' magnetic plasmon modes can be observed in angle-resolved CL spectra.

The previous section built up intuition on the directionality of light scattered by the magnetic modes of the 2-mer and 3-mer. This intuition informs the particular angles at which to collect CL spectra. Fig. 4 shows simulated point angle-resolved CL spectra of the 2-mer and 3-mer, with the electron beam position chosen so as to excite the aN (blue) and NS (orange) modes. Note however, due to the symmetry of the oligomers, the blue electron beam position excites not only the aN mode, but also weakly the NS mode. Since the radiation profile of the aN mode is orthogonal to that of the NS mode, it is possible to distinguish

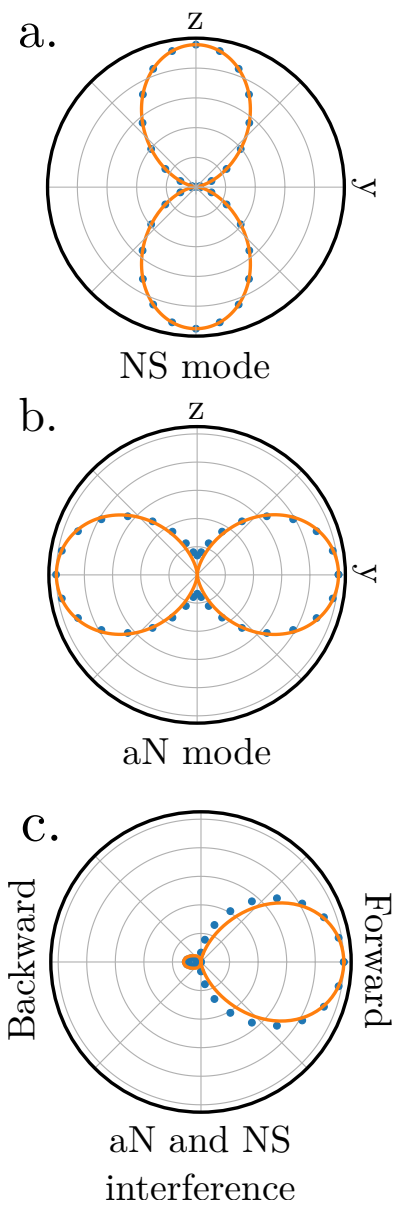

Figure 3: Magnetic field distributions of a magnetic dipole mode (a) and an electric dipole mode (c) in the xy-plane with corresponding radiation patterns (b and d) in the yz-plane. The magnetic dipole exhibits the expected dipolar doughnut, or two lobe, shape with a node along the z-axis. The electric dipole moment also shows the expected pattern with a node along the y-axis.

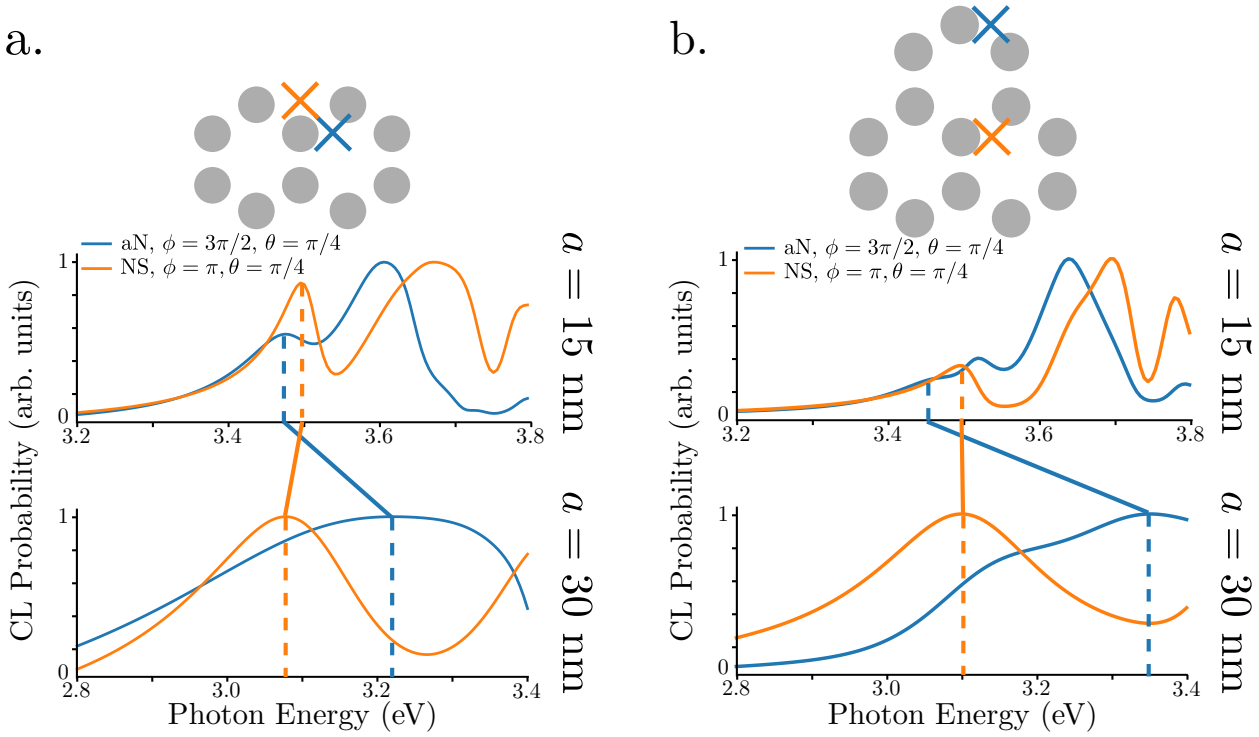

Figure 4: Angle-resolved cathodoluminescence spectra of the 2mer (a and b) and 3mer (c and d). By choosing the beam positions marked on the diagrams and choosing different angles at which to measure the light emitted, the magnetic modes of each oligomer can be disentangled. The colored "x's" correspond to colored traces. The blue traces show a collection angle of $\phi = 3\pi/2$ and the orange traces are for $\phi = \pi$, while both have $\theta = \pi/4$. Simulating these CL experiments with $r_0 = 15$ nm shows the aN modes lower in energy than the NS modes, as predicted. WIth $r_0 = 30$ nm, the modes switch, again as predicted.

them by analyzing the angular distribution of emitted CL radiation. The angle-resolved CL spectra at two such angles are reported in Fig. 4. These simulated spectra confirm the predictions of the model displayed in Fig. 2; specifically, between $a = 15 - 30$ nm, the aN and NS modes switch spectral order. The simulation also shows mode switching at $a \approx 7$ nm, however, the splitting energies are too small to be experimentally detectable with conventional CL. Nevertheless, experimental confirmation of the secondary mode splitting is possible, and would verify both our analytical and numerical predictions.

4 Magnetic Plasmon Resonances in Hexagonally-Packed Nanoclusters

Ref.[15] synthesizes and optically characterizes hexagonally-packed nanoclusters composed of noble metal nanoparticles in the intermediate size regime, between few particle nanoclusters and infinite arrays. Here, we apply our analytical modeling and numerical simulation to investigate the behavior of the magnetic plasmon resonances in these systems as a function of size, with an eye toward engineering magnetic resonances at particular resonance energies. Such tunability may be important in the design of future negative index materials with spectral tunability. Specifically, we consider hexagonally packed clusters composed of 13, 19, and 31 MNPs displayed in Fig. 5 as well as the insets of Fig. 6.

Fig. 5 displays the signed magnetic field magnitude of the aN (panel a) and NS (panel c) magnetic plasmon resonances of the 13-, 19-, and 31-particle nanoclusters. The black arrows denote the electric dipole moments of the individual MNPs within each magnetic plasmon mode, the magenta arrows denote the net electric dipole moment of the nanocluster, and the background color denotes the strength of the associated magnetic field. The net electric or magnetic dipole magnitude is denoted below each panel. Panels b and d display the energy-filtered electron energy-loss (EEL) profiles of these modes. It is important to note that each aN mode is weakly excitable from the middle MNP (as indicated by the low EEL

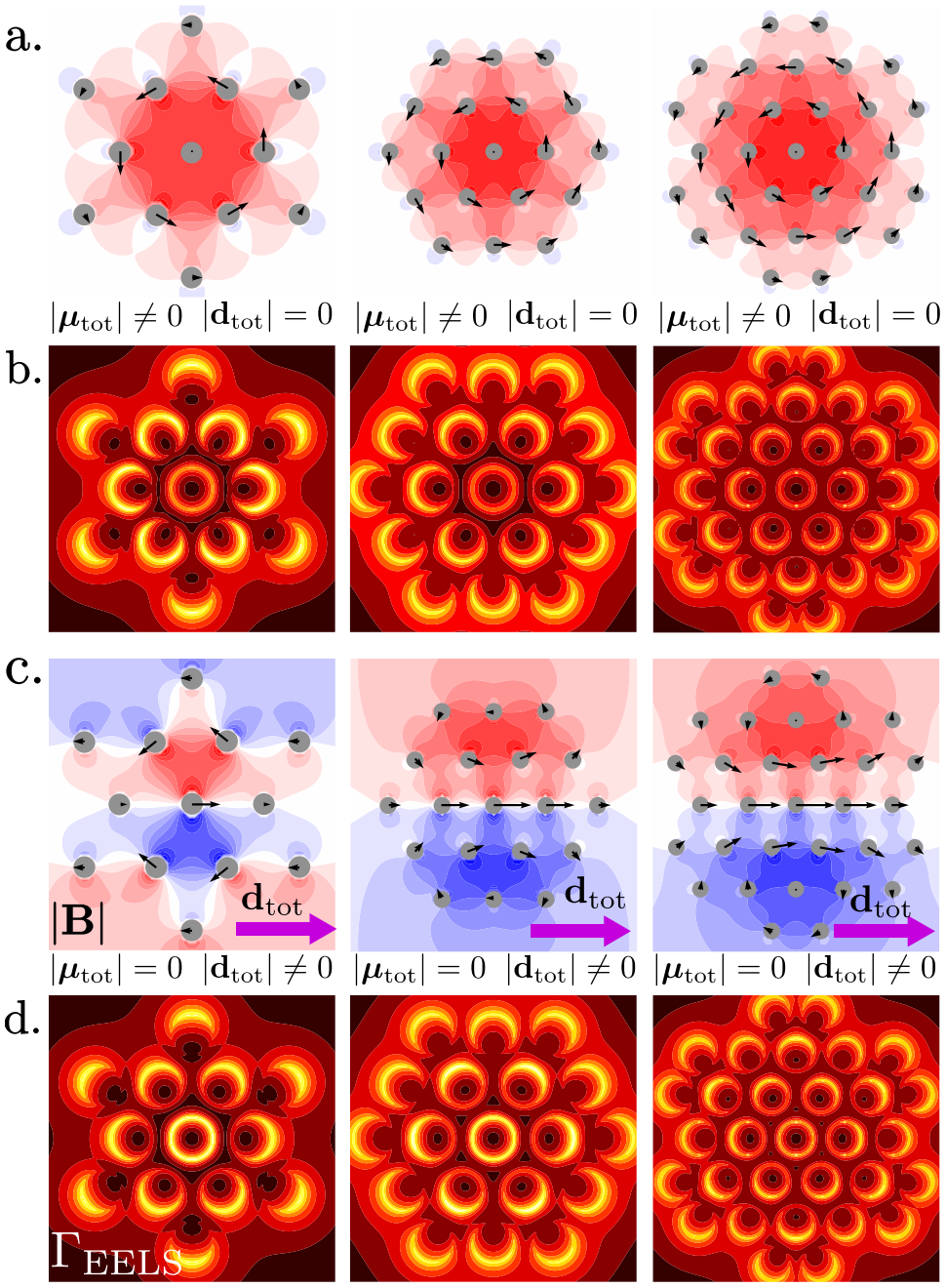

Figure 5: Signed magnetic field magnitudes of the modes of the 13-particle (a, b, and c), 19-particle (d, e, and f), and 31-particle (g, h, and i) clusters. Similarly to the 2mer and 3mer from before, we present only those magnetic modes with either NS and electric dipole character (a, b, d, e, g, and h) or with aN and magnetic dipole character (c, f, and i).

probability surrounding it), while the NS mode is strongly excitable from the same location (as indicated by the high EEL probability surrounding it). In all cases, the NS mode is doubly degenerate as would be true of any structure with sixfold symmetry. In analogy to the oligomers, these magnetic modes are chosen because they are the simplest (i.e., lowest order) and their radiation patterns are spatially orthogonal.

Fig. 6 displays the evolution of the aN and NS magnetic resonances with size a as dictated by the model. Here the size-dependent behavior of the nanocluster resonances is different due to the hexagonal packing as opposed to the open-ring structure of the N-mer. Nevertheless, the analytic model is capable of predicting the magnetic spectrum. Most surprising is the oscillatory behavior of the nanoclusters' magnetic resonances with size as opposed to the expected monotonic redshifting of those of the N-mer (see Fig. 2). Panels b and c display the total interaction energy U, and its near-, intermediate-, and far-field contributions, showing that this oscillatory behavior is due to retardation effects through the $e^{ikr_{ij}}$ factor in Eq. (2).

Figure 7 shows simulated angle-resolved CL spectra for the 13-, 19-, and 31-particle nanoclusters acquired at the two indicated beam positions and collection angles. Inspection of the EEL maps of the NS and aN magnetic resonances in panels b and d of Fig. 5 indicates the optimal electron beam positions to excite each magnetic plamson mode, i.e., those positions with highest EEL probability. In particular, the NS mode (Fig. 5c) is most easily excited near the central MNP, while the aN mode (Fig. 5a) is more easily excited from the outer MNPs surrounding the central MNP. In addition, the radiative profile of each mode helps to identify the two magnetic resonances of interest. Because the aN mode radiates strongly in the xy-plane, and weakly in the z-direction, it is most easily detected at angles between $0 < \theta < \pi/2$. Alternatively, the NS mode is detected either for angles very close to the backward scattering direction ($\theta \approx 0$), or parallel to the impact plane (here, the y-direction for this particular beam position). The aN beam position also weakly excites the degenerate NS modes, meaning the corresponding CL spectrum will provide a secondary

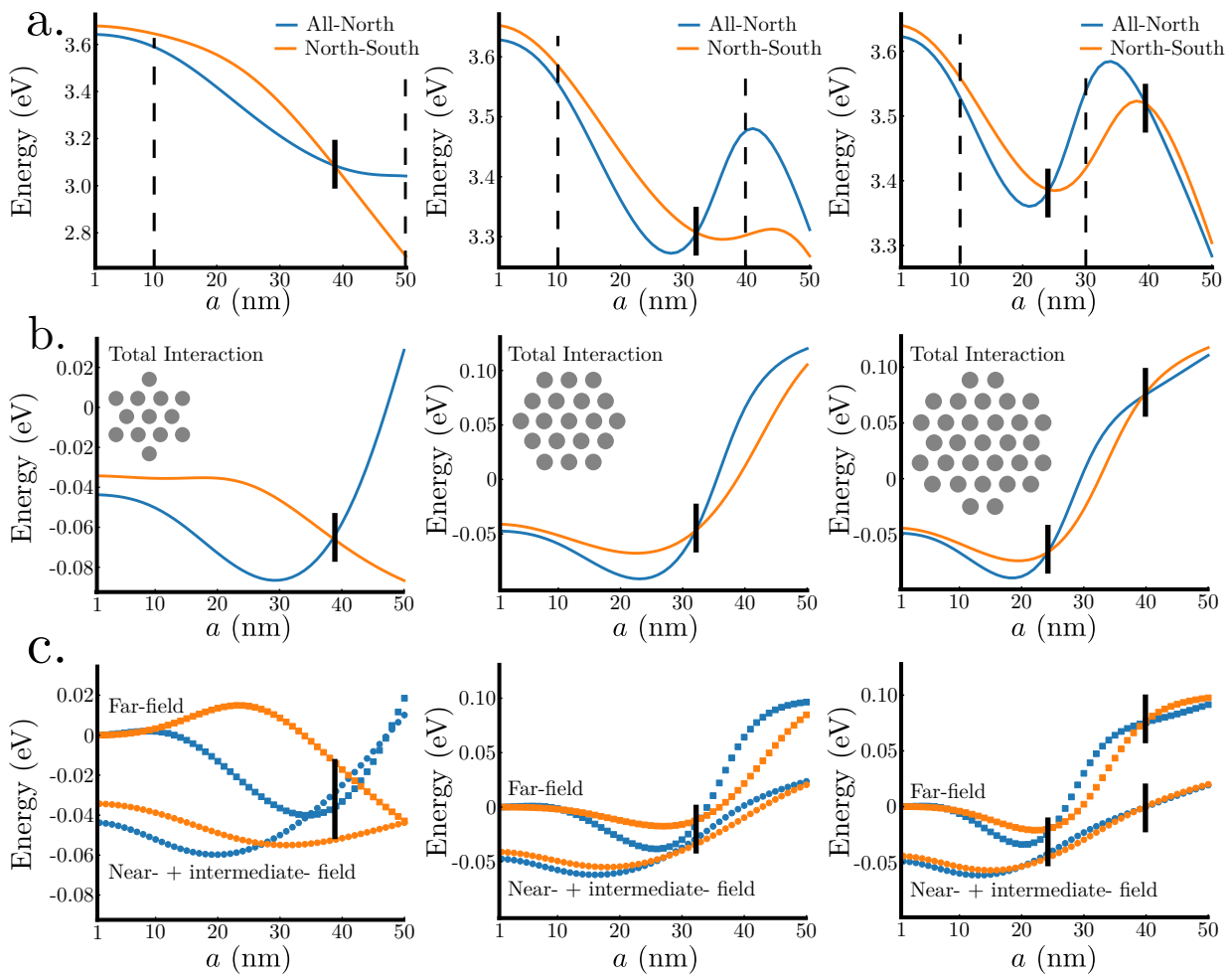

Figure 6: Eigenenergies and interaction energies for the magnetic modes of the 13- (a and b), 19- (c and d), and 31-particle (e and f) clusters. Unlike the 2mer and 3mer, at very small values of r_0, the aN modes are lower in energy than the NS modes. However, for each system a crossing point does occur between $r_0 = 30$ nm and $r_0 = 40$ nm. While the modes of the 13-particle system behave as expected, the aN and NS modes of the larger clusters behave contrary to the intuition built from the earlier model systems. At larger sizes, instead of a monotonic decrease in eigenenergies, the modes exhibit an increase in energy. Looking at the interaction energies, it becomes clear that this is again due to retardation effects, as the term that contributes the most anti-bonding character to the total interaction energy is the far-field. Furthermore, the 31-particle system exhibits a second crossing, unlike the other two structures, and the increase in its eigenenergies is maximized at smaller sizes.

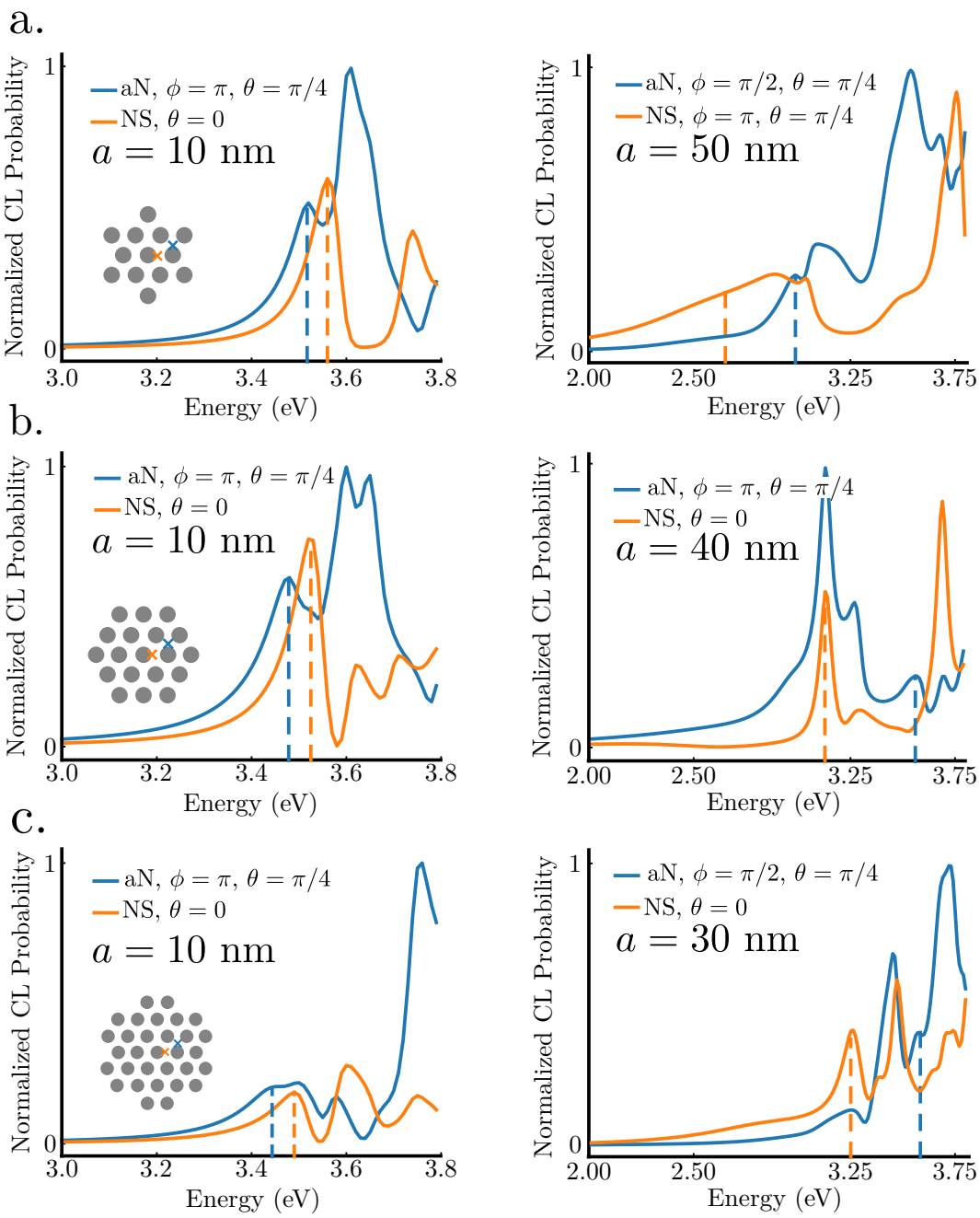

Figure 7: Simulated angle-resolved cathodoluminescence spectra of the 13-, 19-, and 31-particle systems. Blue spectra were acquired at the beam positions marked with a blue x in order to preferentially excite the aN mode. Orange spectra were collected at the points marked with an orange x in order to preferentially excite the x-polarized NS mode. Spectra for the 13-particle aggregate were computed for $r_0 = 10$ nm (a) and $r_0 = 50$ nm (b). Spectra for the 19-particle aggregate were computed for $r_0 = 10$ nm (c) and $r_0 = 40$ nm (d). Spectra for the 31-particle aggregate were computed for $r_0 = 10$ nm (e) and $r_0 = 30$ nm (f). The dashed lines in each spectrum indicate the peak location of the aN modes (blue curves) and the NS modes (orange curves). Each panel also displays the collection angles for each spectrum.

signature of the spectral location of that mode. This fact is evident in multiple simulated CL spectra displayed in Figs. 4 and 7.

5 Conclusion

This paper is concluded.

6 Methods

Here we show the equations of motion describing magnetic plasmon resonances in nanoparticle clusters. Refs.[7] and[48] describe how to map the solutions of Maxwell's Equations for electric plasmon resonances onto mechanical oscillators with effective masses. The resulting Hamiltonian for a system of N frictionless coupled oscillators is

$$H = \sum_i \frac{\mathbf{p}_i^2}{2m_{\rm sp}} + \frac{1}{2} m_{\rm sp}\omega_{\rm sp}^2 \mathbf{q}_i^2 - \frac{e}{2} \sum_{ij, i\neq j} \mathbf{q}_i \cdot \mathbf{E}_j(\mathbf{r}_i), \tag{7}$$

where $\mathbf{q}_i$ and $\mathbf{p}_i$ are the coordinate and momentum of the ith plasmon oscillator located at $\mathbf{r}_i$ with effective mass $m_{\rm sp}$ and resonance frequency $\omega_{\rm sp}$, defined previosuly. $\mathbf{E}_j(\mathbf{r}_i)$ is the full electric dipole field presented in Eq. 2. The resulting equations of motion are,

$$\ddot{\mathbf{q}}_i = -\omega_{\rm sp}^2 \mathbf{q}_i + \frac{e}{m_{\rm sp}} \sum_{j\neq i} \mathbf{E}_j(\mathbf{r}_i, \omega) \tag{8}$$

which is Eq. 1. Assuming sinusoidal oscillation in time and rewriting the electric field in terms of the plasmon coordinate results in the equations of motion

$$(\omega_{\rm sp}^2 - \omega^2)\mathbf{q}_i - \frac{e^2}{m_{\rm sp}} \sum_{j\neq i} \mathbf{\Lambda}_{ij}(\omega) \cdot \mathbf{q}_j = 0. \tag{9}$$

It is this system of equations for the plasmon oscillator coordinates that we solve to determine the magnetic plasmon resonances. Considering two identical, coupled, collinear oscillators as an example and projecting out the directional-dependence, Eq. 9 becomes

$$\begin{aligned}(\omega_{\mathrm{sp}}^2 - \omega^2)q_1 - g_{12}(\omega)q_2 = 0 \\ (\omega_{\mathrm{sp}}^2 - \omega^2)q_2 - g_{12}(\omega)q_1 = 0,\end{aligned} \tag{10}$$

or, equivalently,

$$\begin{bmatrix}\omega_{\mathrm{sp}}^2 - \omega^2 & -g_{12}(\omega) \\ -g_{12}(\omega) & \omega_{\mathrm{sp}}^2 - \omega^2\end{bmatrix}\begin{bmatrix}q_1 \\ q_2\end{bmatrix} = \begin{bmatrix}0 \\ 0\end{bmatrix}. \tag{11}$$

where $g_{12} = -e^2/m_{\mathrm{sp}}(2r_{12}^{-3} - 2ikr_{12}^{-2})$. Solution of this system produces the hybridized plasmon resonance frequencies and modes of the dimer. Specifically, they are

$$\omega_{\pm} = \sqrt{\omega_{\mathrm{sp}}^2 \pm g_{12}(\omega)} \tag{12}$$

and

$$q_{\pm} = \frac{1}{\sqrt{2}}\left(q_1 \pm q_2\right). \tag{13}$$

Note that the coupling term $g_{12}(\omega)$ is frequency dependent, meaning that the eigenvalue problem must be solved iteratively until convergence. The magnetic plasmon resonances described herein are obtained as a straightforward extension of this dimer example.

Acknowledgement

This work was supported by the U.S. Department of Energy Basic Energy Sciences under award number DE-SC0018040 (D.J.M.) and by the State of Washington through the University of Washington Clean Energy Institute and via funding from the Washington Research Foundation (N.P.M.). This work was facilitated through the use of advanced computational, storage, and networking infrastructure provided by the Hyak supercomputer system and

funded by the STF at the University of Washington. N.P.M. would like to thank Dr. Niket Thakkar and Harrison Goldwyn for helpful discussions and advice.

References

(1) Prodan, E.; Radloff, C.; Halas, N. J.; Nordlander, P. A Hybridization Model for the Plasmon Response of Complex Nanostructures. *Science* **2003**, *302*, 419–422.

(2) Magnetic resonance in metal nanoantennas. 2004; pp 5508 – 5508 – 10.

(3) Alù, A.; Salandrino, A.; Engheta, N. Negative effective permeability and left-handed materials at optical frequencies. *Opt. Express* **2006**, *14*, 1557–1567.

(4) Alù, A.; Engheta, N. Dynamical theory of artificial optical magnetism produced by rings of plasmonic nanoparticles. *Phys. Rev. B* **2008**, *78*, 085112.

(5) Hentschel, M.; Dregely, D.; Vogelgesang, R.; Giessen, H.; Liu, N. Plasmonic oligomers: The role of individual particles in collective behavior. *ACS Nano* **2011**, *5*, 2042–2050.

(6) Sheikholeslami, S. N.; García-Etxarri, A.; Dionne, J. A. Controlling the interplay of electric and magnetic modes via Fano-like plasmon resonances. *Nano Lett.* **2011**, *11*, 3927–3934.

(7) Cherqui, C.; Bigelow, N. W.; Vaschillo, A.; Goldwyn, H.; Masiello, D. J. Combined tight-binding and numerical electrodynamics understanding of the STEM/EELS magneto-optical responses of aromatic plasmon-supporting metal oligomers. *ACS Photonics* **2014**, *1*, 1013–1024.

(8) Qian, Z.; Hastings, S. P.; Li, C.; Edward, B.; McGinn, C. K.; Engheta, N.; Fakhraai, Z.; Park, S.-J. Raspberry-like metamolecules exhibiting strong magnetic resonances. *ACS Nano* **2015**, *9*, 1263–1270.

(9) Scholl, J. A.; García-Etxarri, A.; Aguirregabiria, G.; Esteban, R.; Narayan, T. C.; Koh, A. L.; Aizpurua, J.; Dionne, J. A. Evolution of plasmonic metamolecule modes in the quantum tunneling regime. *ACS Nano* **2016**, *10*, 1346–1354.

(10) Cherqui, C.; Wu, Y.; Li, G.; Quillin, S. C.; Busche, J. A.; Thakkar, N.; West, C. A.; Montoni, N. P.; Rack, P. D.; Camden, J. P. .; Masiello, D. J. STEM/EELS imaging of magnetic hybridization in symmetric and symmetry-broken plasmon oligomer dimers and all-magnetic fano interference. *Nano Lett.* **2016**, *16*, 6668–6676.

(11) Liu, H.; Genov, D. A.; Wu, D. M.; Liu, Y. M.; Steele, J. M.; Sun, C.; Zhu, S. N.; Zhang, X. Magnetic plasmon propagation along a chain of connected subwavelength resonators at infrared frequencies. *Phys. Rev. Lett.* **2006**, *97*, 243902.

(12) Liu, H.; Genov, D. A.; Wu, D. M.; Liu, Y. M.; Liu, Z. W.; Sun, C.; Zhu, S. N.; Zhang, X. Magnetic plasmon hybridization and optical activity at optical frequencies in metallic nanostructures. *Phys. Rev. B* **2007**, *76*, 073101.

(13) Liu, N.; Mukherjee, S.; Bao, K.; Brown, L. V.; Dorfmüller, J.; Nordlander, P.; Halas, N. J. Magnetic plasmon formation and propagation in artificial aromatic molecules. *Nano Lett.* **2011**, *12*, 364–369.

(14) Liu, N.; Mukherjee, S.; Bao, K.; Li, Y.; Brown, L. V.; Nordlander, P.; Halas, N. J. Manipulating magnetic plasmon propagation in metallic nanocluster networks. *ACS Nano* **2012**, *6*, 5482–5488.

(15) Greybush, N. J.; Liberal, I. n.; Malassis, L.; Kikkawa, J. M.; Engheta, N.; Murray, C. B.; Kagan, C. R. Plasmon resonances in self-assembled two-dimensional Au nanocrystal metamolecules. *ACS Nano* **2017**, *11*, 2917–2927.

(16) Brandl, D. W.; Mirin, N. A.; Nordlander, P. Plasmon modes of nanosphere trimers and quadrumers. *J. Phys. Chem. B* **2006**, *110*, 12302–12310.

(17) Darvishzadeh-Varcheie, M.; Guclu, C.; Capolino, F. Magnetic nanoantennas made of plasmonic nanoclusters for photoinduced magnetic field enhancement. *Phys. Rev. Appl.* **2017**, *8*, 024033.

(18) Haynes, C. L.; McFarland, A. D.; Zhao, L.; Van Duyne, R. P.; Schatz, G. C.; Gunnarsson, L.; Prikulis, J.; Kasemo, B.; Käll, M. Nanoparticle optics: the importance of radiative dipole coupling in two-dimensional nanoparticle arrays. *J. Phys. Chem. B* **2003**, *107*, 7337–7342.

(19) Weick, G.; Woollacott, C.; Barnes, W. L.; Hess, O.; Mariani, E. Dirac-like plasmons in honeycomb lattices of metallic nanoparticles. *Phys. Rev. Lett.* **2013**, *110*, 106801.

(20) Li, C.; Lee, S.; Qian, Z.; Woods, C.; Park, S.-J.; Fakhraai, Z. Controlling Magnetic Dipole Resonance in Raspberry-like Metamolecules. *The Journal of Physical Chemistry C* **2018**, *122*, 6808–6817.

(21) Optical magnetism in core-satellite nanostructures excited by vector beams. 2018; pp 10541 – 10541 – 9.

(22) Turner, M. D.; Hossain, M. M.; Gu, M. The effects of retardation on plasmon hybridization within metallic nanostructures. *New J. Phys.* **2010**, *12*, 083062.

(23) Nordlander, P.; Oubre, C.; Prodan, E.; Li, K.; Stockman, M. I. Plasmon hybridization in nanoparticle dimers. *Nano Lett.* **2004**, *4*, 899–903.

(24) Dahmen, C.; Schmidt, B.; von Plessen, G. Radiation damping in metal nanoparticle pairs. *Nano Lett.* **2007**, *7*, 318–322.

(25) Clippe, P.; Evrard, R.; Lucas, A. A. Aggregation effect on the infrared absorption spectrum of small ionic crystals. *Phys. Rev. B* **1976**, *14*, 1715–1721.

(26) Aravind, P.; Nitzan, A.; Metiu, H. The interaction between electromagnetic resonances

and its role in spectroscopic studies of molecules adsorbed on colloidal particles or metal spheres. *Surf. Sci.* **1981**, *110*, 189 – 204.

(27) Kottmann, J. P.; Martin, O. J. F. Retardation-induced plasmon resonances in coupled nanoparticles. *Opt. Lett.* **2001**, 1096–1098.

(28) Prodan, E.; Radloff, C.; Halas, N. J.; Nordlander, P. A hybridization model for the plasmon response of complex nanostructures. *Science* **2003**, *302*, 419–422.

(29) Prodan, E.; Nordlander, P. Plasmon hybridization in spherical nanoparticles. *J. of Chem. Phys.* **2004**, *120*, 5444–5454.

(30) Rechberger, W.; Hohenau, A.; Leitner, A.; Krenn, J.; Lamprecht, B.; Aussenegg, F. Optical properties of two interacting gold nanoparticles. *Opt. Commun.* **2003**, *220*, 137 – 141.

(31) Bouhelier, A.; Bachelot, R.; Im, J. S.; Wiederrecht, G. P.; Lerondel, G.; Kostcheev, S.; Royer, P. Electromagnetic interactions in plasmonic nanoparticle arrays. *J. Phys. Chem. B* **2005**, *109*, 3195–3198.

(32) Myroshnychenko, V.; Rodriguez-Fernandez, J.; Pastoriza-Santos, I.; Funston, A. M.; Novo, C.; Mulvaney, P.; Liz-Marzan, L. M.; Garcia de Abajo, F. J. Modelling the optical response of gold nanoparticles. *Chem. Soc. Rev.* **2008**, *37*, 1792–1805.

(33) Davis, T. J.; Vernon, K. C.; Gómez, D. E. Designing plasmonic systems using optical coupling between nanoparticles. *Phys. Rev. B* **2009**, *79*, 155423.

(34) Kinnan, M. K.; Chumanov, G. Plasmon coupling in two-dimensional arrays of silver nanoparticles: II. Effect of the particle size and interparticle distance. *J. Phys. Chem. C* **2010**, *114*, 7496–7501.

(35) Kravets, V. V.; Pinchuk, A. O. Near-, middle-, and far-field dipolar interactions in gold nanoparticle arrays. *Proc. SPIE* **2016**, *9724*, 97240B–97240B–8.

(36) Hohenester, U. Simulating electron energy loss spectroscopy with the MNPBEM toolbox. *Comp. Phys. Comm.* **2014**, *185*, 1177 – 1187.

(37) Coenen, T.; Vesseur, E. J. R.; Polman, A.; Koenderink, A. F. Directional emission from plasmonic YagiâĂŞUda antennas probed by angle-resolved cathodoluminescence spectroscopy. *Nano Lett.* **2011**, *11*, 3779–3784.

(38) Coenen, T.; Vesseur, E. J. R.; Polman, A. Angle-resolved cathodoluminescence spectroscopy. *Appl. Phys. Lett.* **2011**, *99*, 143103.

(39) Coenen, T.; Bernal Arango, F.; Femius Koenderink, A.; Polman, A. Directional emission from a single plasmonic scatterer. *Nat. Comm.* **2014**, *5*, 3250.

(40) Pendry, J. B. Focus issue: negative refraction and metamaterials. *Opt. Express* **2003**, *11*, 639–639.

(41) Fang, N.; Lee, H.; Sun, C.; Zhang, X. Sub-diffraction-limited optical imaging with a silver superlens. *Science* **2005**, *308*, 534–537.

(42) Cai, W.; Chettiar, U. K.; Kildishev, A. V.; Shalaev, V. M. Optical cloaking with metamaterials. *Nature Photonics* **2007**, *1*, 224.

(43) Pinchuk, A. O.; Schatz, G. C. Metamaterials with gradient negative index of refraction. *J. Opt. Soc. Am. A* **2007**, *24*, A39–A44.

(44) Shalaev, V. M. Transforming light. *Science* **2008**, *322*, 376–379.

(45) Valentine, J.; Zhang, S.; Zentgraf, T.; Ulin-Avila, E.; Genov, D. A.; Bartal, G.; Zhang, X. Three-dimensional optical metamaterial with a negative refractive index. *Nature* **2008**, *455*, 376–379.

(46) Ferrari, J. A.; Perciante, C. D. Superlenses, metamaterials, and negative refraction. *J. Opt. Soc. Am. A* **2009**, *26*, 78–84.

(47) Chen, S.; Zhang, Y.; Shih, T.-M.; Yang, W.; Hu, S.; Hu, X.; Li, J.; Ren, B.; Mao, B.; Yang, Z.; Tian, Z. Plasmon-Induced Magnetic Resonance Enhanced Raman Spectroscopy. *Nano Letters* **0**, *0*, null, PMID: 29504760.

(48) Cherqui, C.; Thakkar, N.; Li, G.; Camden, J. P.; Masiello, D. J. Characterizing localized surface plasmons using electron energy-loss spectroscopy. *Ann. Rev. Phys. Chem.* **2016**, *67*, 331–357.

(49) Purcell, E. M.; Pennypacker, C. R. Scattering and absorption of light by nonspherical dielectric grains. *Astrophys. J.* **1973**, *186*, 705–714.

(50) Hohenester, U.; Trügler, A. MNPBEM - A matlab toolbox for the simulation of plasmonic nanoparticles. *Comp. Phys. Comm.* **2012**, *183*, 370 – 381.

(51) Jain, P. K.; El-Sayed, M. A. Noble metal nanoparticle pairs: effect of medium for enhanced nanosensing. *Nano Lett.* **2008**, *8*, 4347–4352.

(52) Jackson, J. D. *Classical Electrodynamics*, 3rd ed.; Wiley: New York, NY, 1999.

(53) Schwinger, J.; Deraad, L.; Milton, K.; Tsai, W.; Norton, J. *Classical Electrodynamics*; Advanced book program; Avalon Publishing, 1998.

(54) Liu, W.; Miroshnichenko, A. E.; Neshev, D. N.; Kivshar, Y. S. Broadband unidirectional scattering by magneto-electric core-shell nanoparticles. *ACS Nano* **2012**, *6*, 5489–5497.

Graphical TOC Entry